ACS Catalysis

pubs.acs.org/acscatalysis

Research Article

# Interfacial Electron Engineering Unlocks Efficient Nitrate Electrosynthesis by Balancing Nitrogen Activation and Oxygen Evolution

Haixia Zeng, Dashuai Wang,* Cheng-Jie Yang, Chung-Li Dong, Weixiao Lin, Xiahan Sang, Bin Yang, Zhongjian Li, Siyu Yao, Qinghua Zhang, Jianguo Lu, Lecheng Lei, Yuanyuan Li, Raul D. Rodriguez, and Yang Hou*

**Cite This:** *ACS Catal.* 2025, 15, 9610−9620

**Read Online**

ACCESS | Metrics & More | Article Recommendations | Supporting Information

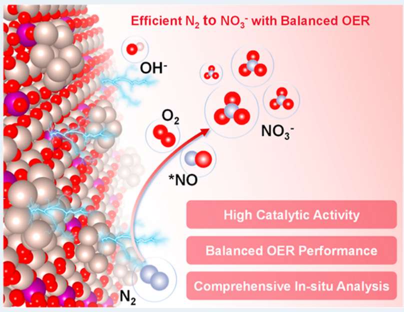

**ABSTRACT:** The electrocatalytic nitrogen oxidation reaction (NOR) represents an environmentally friendly alternative to the energy-intensive industrial synthesis of nitrate, traditionally derived from ammonia produced via the Haber−Bosch process. The primary challenges in electrocatalytic NOR revolve around the effective activation of inert nitrogen and achieving a suitable oxygen evolution reaction (OER). To address these challenges, the development of advanced electrocatalysts capable of efficiently adsorbing and activating nitrogen while simultaneously modulating the OER activity is paramount for advancing electrochemical NOR technologies. This work innovatively integrated Ru clusters with Mn-doped $RuO_2$, balancing NOR and OER through interfacial electron transfer at Ru/$Mn_x$-$RuO_2$ grain boundaries. The incorporation of Mn into $RuO_2$ elevated the OER reaction energy to 0.630 eV, compared to 0.568 eV for pristine $RuO_2$, while simultaneously enhancing nitrogen adsorption and activation on the Ru clusters. This synergistic effect resulted in an optimized NOR performance. The engineered Ru/$Mn_{1.04}$-$RuO_2$ exhibited positive catalytic efficiency for NOR, achieving a record-high nitrate yield of 52.6 $\mu$g $mg^{-1}$ $h^{-1}$ and a Faraday efficiency of 44.29% under alkaline conditions, demonstrating significant progress toward viable electrochemical nitrate production.

**KEYWORDS:** *electrocatalytic nitrogen oxidation, interfacial electron transfer, cooperative interaction, nitrate electrosynthesis, competing oxygen evolution reaction*

## 1. INTRODUCTION

Nitrate products are indispensable in various human activities, serving as essential components in agricultural fertilizers and as key oxidizing agents in the synthesis of explosives.[1,2] Conventionally, nitrate and nitric acid are produced through the Ostwald process, a multistep procedure that involves the oxidation of ammonia to nitric acid. The ammonia required for this process is predominantly synthesized via the Haber−Bosch method. Both of these industrial processes operate under extreme conditions of high temperature and pressure, resulting in substantial energy consumption and significant $CO_2$ emissions.[3−5] Given the escalating concerns over energy sustainability and environmental impact, the development of ecofriendly and sustainable technologies for nitrate production is not only desirable but imperative.

In recent years, electrosynthesis reactions have emerged as a transformative approach for producing high-value-added chemical products under mild conditions.[6−11] Among these, the electrochemical nitrogen reduction reaction for ammonia synthesis has been extensively investigated as a sustainable alternative to the conventional Haber−Bosch process, which laid foundational knowledge for the exploration of the nitrogen oxidation reaction (NOR), given that both reactions involve the activation of nitrogen.[1,8,12−15] NOR offers a compelling pathway for nitrate synthesis, operating at ambient temperature and pressure while utilizing renewable electricity, thereby presenting a promising and sustainable alternative to traditional nitric acid and nitrate production methods.[16,17] However, despite its potential, the practical implementation of high-efficiency NOR faces significant challenges, primarily due to the competing four-electron oxygen evolution reaction (OER) at the anode, which severely limits its overall efficiency and selectivity.[18,19]

The electrocatalytic NOR process comprises two fundamental steps: (1) the adsorption and activation of nitrogen molecules on metal active sites, leading to the formation of *NO intermediates, and (2) the subsequent nonelectrochem-

**Received:** March 5, 2025
**Revised:** May 8, 2025
**Accepted:** May 13, 2025
**Published:** May 21, 2025

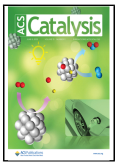

https://doi.org/10.1021/acscatal.5c01568

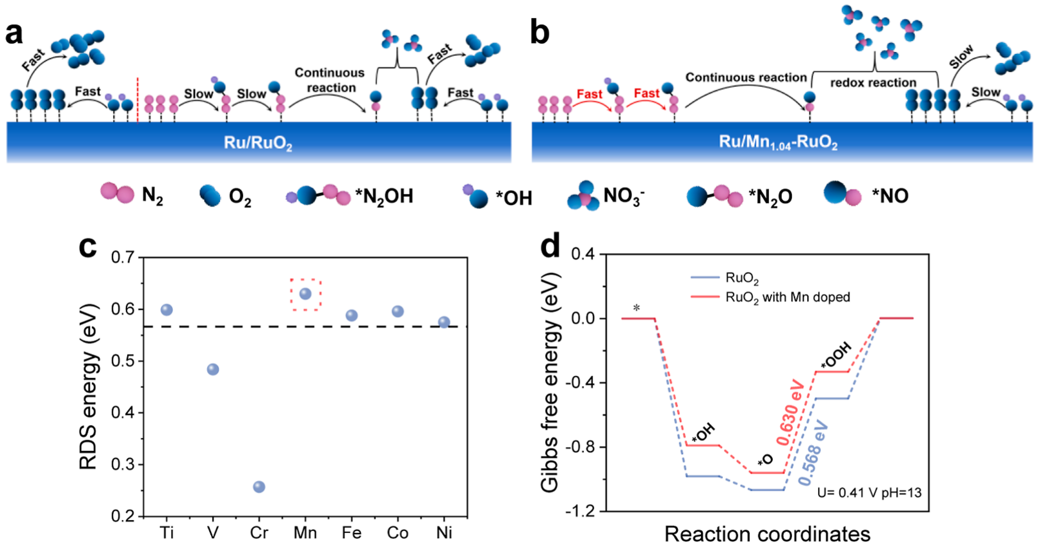

**Figure 1.** DFT-guided screening of the catalysts and NOR pathway illustration. Schematic illustration of the NOR occurring on (a) Ru/RuO$_2$ and (b) Ru/Mn$_{1.04}$-RuO$_2$. (c) The RDS energies of the OER on RuO$_2$(110) surfaces doped with various metals. (d) Comparisons of the OER properties on RuO$_2$(110) before and after Mn doping.

ical redox reaction of these *NO intermediates with O$_2$ generated via the OER to produce nitrate.[18−20] To achieve high efficiency in electrosynthetic nitrate production, it is essential to develop advanced electrocatalysts that not only exhibit strong capabilities for nitrogen adsorption and activation but also provide optimized OER activity. Balancing these dual functionalities is critical to maximizing the NOR performance.

Recently, a range of catalysts, including noble metals, transition-metal oxides, and metal-free materials, have been explored as potential electrocatalysts for the NOR.[4,18,20−28] Among these, Kuang et al. proposed an efficient strategy to integrate the OER with the NOR process within a single catalytic system using Ru-doped TiO$_2$/RuO$_2$ as the electrocatalyst.[18] Similarly, Xu et al. demonstrated that cation vacancy-rich RuO$_2$ exhibits exceptional NOR performance, primarily due to its optimized balance between OER and NOR activities.[28] These studies collectively highlight the intrinsic interplay between the NOR and the OER, offering a strategic pathway to reconcile their competing demands. However, despite these significant advancements, prior research has yet to fully unravel the mechanisms by which catalysts efficiently modulate the OER process to influence NOR-specific reaction pathways. Furthermore, the detailed reaction mechanisms and precise pathways governing the NOR remain inadequately explained.

In this study, we engineered a novel Ru/Mn$_{1.04}$-RuO$_2$ catalyst, wherein Ru clusters function as the primary active sites for nitrogen adsorption and activation, while RuO$_2$ facilitates the OER. The incorporation of Mn dopants strategically elevates the reaction energy for the OER on RuO$_2$ while simultaneously lowering the reaction energy for nitrogen adsorption and activation on Ru clusters. This dual modulation was engineered to enhance the catalyst's selectivity toward the NOR, thereby maximizing its efficiency for nitrate synthesis. Through a combination of theoretical calculations and experimental validation, we demonstrated that the Ru/Mn$_{1.04}$-RuO$_2$ catalyst not only increases the reaction energy for the OER but also reduces the reaction energy for the formation of *N$_2$O, identified as the rate-determining step (RDS) of NOR, thus resulting in a remarkable improvement in both the Faraday efficiency (FE) and nitrate yield (Figure 1a,b).

## 2. RESULTS AND DISCUSSION

### 2.1. Structural Design of the NOR Catalyst via Theoretical Calculations.

Building on prior research, nitrogen has been shown to exhibit a pronounced affinity for adsorption and activation on noble metal surfaces.[4,18,22,29,30] To identify the most suitable noble metal for this purpose, density functional theory (DFT) calculations were conducted to systematically evaluate the nitrogen adsorption and activation capabilities on Au, Pd, Pt, Rh, Ir, and Ru surfaces. As illustrated in Figure S1, Ru exhibits the lowest adsorption free energy for nitrogen, indicating its superior capacity for nitrogen adsorption and activation among the tested metals. Further analysis using crystal orbital Hamilton population (COHP) revealed a significant weakening of the N−N bond in *N$_2$ on the Ru surface, as reflected by the lowest integral of the COHP (ICOHP) value (Figures S1 and S2). This weakening of the N−N bond is critical for facilitating subsequent steps in the NOR process.[31−35] Given its exceptional activity and relative cost-effectiveness, metallic Ru emerges as the preferred catalyst for nitrogen adsorption and activation.

For the OER, RuO$_2$ was selected as the catalyst due to its well-documented excellent catalytic properties.[32−35] However, its strong OER activity is anticipated to compromise its performance in the NOR,[18,28,36] necessitating strategic modulation to better align with the NOR process. To address this, we explored the modulation of the OER activity on RuO$_2$ through transition metal doping. DFT calculations were employed to compare the RDS energies of the OER across various dopants (as shown in Figure S3, the reaction mechanism of the OER was determined to be AEM through a pH-independent test). As shown in Figures 1c,d and S4−S6, Mn-doped RuO$_2$ exhibits a significantly higher RDS energy of 0.630 eV compared to other metal dopants, indicating that Mn doping effectively moderates the OER activity.[37]

Further analysis of the OER properties on RuO$_2$ (110) before and after Mn doping (Figure 1d) reveals that the RDS energy for the reaction *O + OH$^-$ → *OOH + e$^-$ on pristine

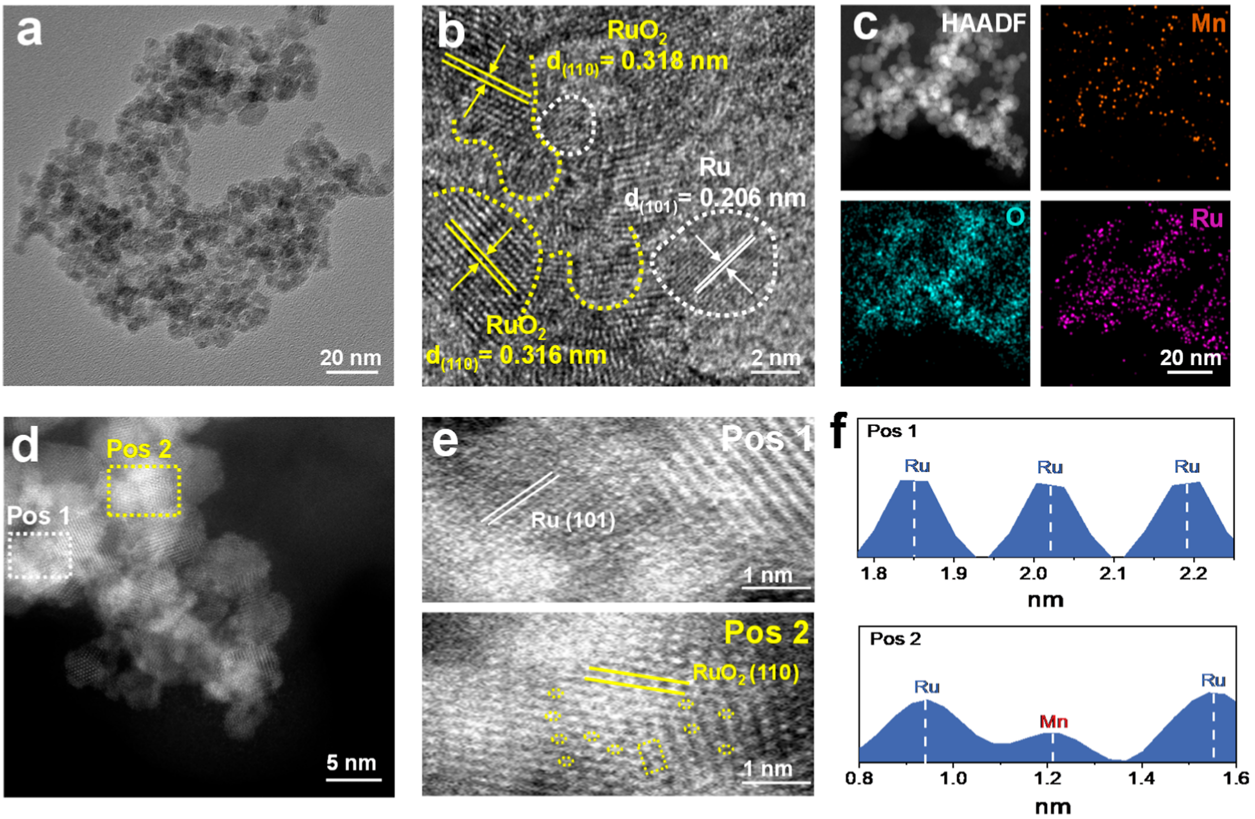

**Figure 2.** Morphological and elemental characterization of Ru/$Mn_{1.04}$-$RuO_2$. (a) TEM, (b) HRTEM, (c) SEM−EDX elemental images of Ru/$Mn_{1.04}$-$RuO_2$ and (d) AC HAADF-STEM image of Ru/$Mn_{1.04}$-$RuO_2$. (e) The enlarged areas of Pos 1 and Pos 2 in (d), with the Mn atoms marked in yellow circles. (f) Atomic intensity profiles along the dashed rectangles in (e).

$RuO_2$ is 0.568 eV, which increases slightly to 0.630 eV upon Mn doping. The detailed mechanisms of the OER occurring on $RuO_2$ and Mn-$RuO_2$ are illustrated in Figures S7 and S8. This moderate increase in RDS energy indicates that Mn-doped $RuO_2$ achieves a balanced OER activity, neither excessively high nor too low, which is essential for enabling efficient nitrate electrosynthesis through the NOR process. In summary, our findings underscore the exceptional capability of Ru metal as an active site for nitrogen adsorption and activation, complemented by Mn-doped $RuO_2$ as a catalyst that provides optimally moderated OER activity.[18,20]

**2.2. Synthesis and Characterization of the NOR Catalyst.** The Ru/$Mn_{1.04}$-$RuO_2$ catalyst was synthesized through a meticulously designed multistep process, combining wet impregnation and controlled calcination (Figure S9).[35] Initially, metal precursors were uniformly impregnated onto a carbon black support by using a wet impregnation method. The resulting material was then subjected to annealing reduction in an $H_2$/Ar atmosphere, leading to the formation of Ru−Mn particles supported on carbon black ($Ru_3Mn_1$/C) (Figure S10). Subsequently, the $Ru_3Mn_1$/C composite was annealed in air, a step that not only oxidized the $Ru_3Mn_1$ particles to form $Ru_3Mn_1O_x$ but also facilitated the complete removal of the carbon black support. Finally, $Ru_3Mn_1O_x$ underwent an acid-leaching treatment to selectively eliminate unstable Mn species, yielding the optimized Ru/$Mn_{1.04}$-$RuO_2$ catalyst.

The structural and compositional characteristics of the prepared catalyst were comprehensively characterized. Scanning electron microscopy (SEM) and transmission electron microscopy (TEM) images (Figures 2a, S11, and S12) revealed that the Ru/$Mn_{1.04}$-$RuO_2$ catalyst exhibited a typical nanoparticle morphology with an average particle diameter ranging from 3 to 7 nm. High-resolution TEM (HRTEM) images further identified distinct crystalline regions corresponding to Ru and $RuO_2$, with well-defined grain boundaries separating these phases. Specifically, lattice spacings of 0.206 and 0.316 nm were assigned to the Ru (101) and $RuO_2$ (110) facets, respectively (Figure 2b),[38] confirming the coexistence of Ru and $RuO_2$ phases within the catalyst structure. This intimate contact at the grain boundaries is critical for facilitating interfacial interactions and enhancing catalytic performance.[39,40] Control samples, including Ru/$RuO_2$, Mn-$RuO_2$, Ru/$Mn_{0.3}$-$RuO_2$, and Ru/$Mn_{2.63}$-$RuO_2$, were synthesized using the same methodology and exhibited morphological features similar to those of Ru/$Mn_{1.04}$-$RuO_2$ (Figure S13). X-ray diffraction (XRD) analysis (Figures S14 and S15) further corroborated the coexistence of Ru (PDF #06-0663) and $RuO_2$ (PDF #40-1290) phases in Ru/$Mn_{1.04}$-$RuO_2$, aligning well with the HRTEM observations. Additionally, scanning electron microscopy−energy-dispersive spectroscopy (SEM−EDX, 1.04 at. %) and inductively coupled plasma-optical emission spectrometry (ICP-OES, 1.09 at. %) confirmed a consistent Mn content in Ru/$Mn_{1.04}$-$RuO_2$ (Figure S16 and Table S1), with the minor variation falling within expected analytical error. EDX elemental mapping images (Figure 2c) demonstrated the homogeneous distribution of Ru, Mn, and O throughout the catalyst, underscoring the uniform incorporation of Mn into the $RuO_2$ matrix.

Aberration-corrected high-angle annular dark-field scanning transmission electron microscopy (AC HAADF-STEM) revealed the atomic-scale spatial distribution of Mn species

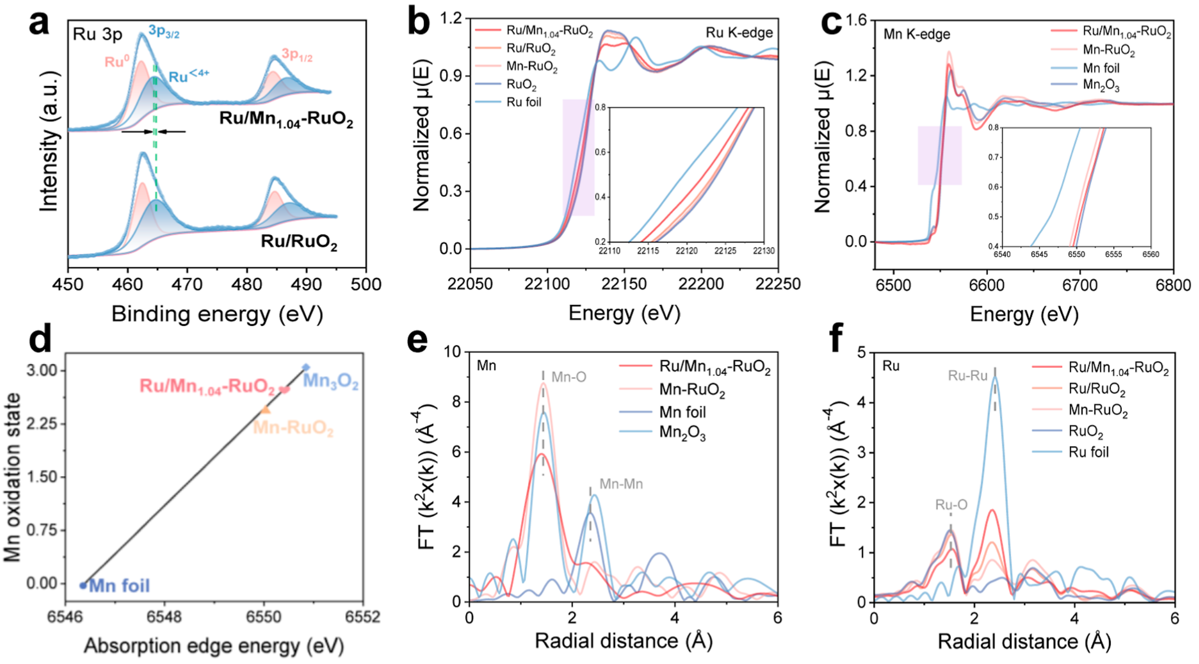

**Figure 3.** Electronic structure and coordination environment characterization of Ru/Mn$_x$-RuO$_2$. (a) Ru 3p XPS spectra of Ru/Mn$_{1.04}$-RuO$_2$ and Mn-RuO$_2$. (b) Normalized XANES spectra of Ru/Mn$_{1.04}$-RuO$_2$, Ru/RuO$_2$, Mn-RuO$_2$, RuO$_2$, and Ru foil at the Ru K-edge; inset: enlarged spectra. (c) Normalized XANES spectra of Ru/Mn$_{1.04}$-RuO$_2$, Mn-RuO$_2$, Mn$_2$O$_3$, and Mn foil at the Mn K-edge; inset: enlarged spectra. (d) The relationship of Mn oxidation state vs adsorption edge energy for Ru/Mn$_{1.04}$-RuO$_2$, Mn-RuO$_2$, Mn$_2$O$_3$, and Mn foil. (e) R-space of the EXAFS spectra at the Mn K-edge for Ru/Mn$_{1.04}$-RuO$_2$, Mn-RuO$_2$, Mn$_2$O$_3$, and Mn foil. (f) R-space of the EXAFS spectra at the Ru K-edge for Ru/Mn$_{1.04}$-RuO$_2$, Ru/RuO$_2$, Mn-RuO$_2$, RuO$_2$, and Ru foil.

within Ru/Mn$_{1.04}$-RuO$_2$ (Figure 2d,e). Two distinct crystallographic domains were resolved: the metallic Ru (101) facet (Pos 1) and the RuO$_2$ (110) phase (Pos 2). Owing to the intrinsic Z-contrast disparity between Mn and Ru, discrete dark contrast features corresponding to isolated Mn atoms were unambiguously identified within the RuO$_2$ lattice.[41,42] Intensity line profiles across the dashed regions (Figure 2f) quantitatively confirmed the homogeneous dispersion of Mn single atoms, exhibiting characteristic intensity reductions relative to those of adjacent Ru columns.

X-ray photoelectron spectroscopy (XPS) investigations revealed pronounced electronic interactions between the Mn and Ru centers within Ru/Mn$_{1.04}$-RuO$_2$ (Figure S17). The Mn 2p$_{3/2}$ core-level spectrum of Ru/Mn$_{1.04}$-RuO$_2$ exhibited a positive binding energy shift relative to Mn-RuO$_2$ control (Figure S18), indicative of electron density depletion at Mn sites.[29] The high-resolution XPS spectra of Ru 3p of the samples could be divided into two peaks located at about 462.3 and 464.5 eV (Figure 3a), which were indexed to Ru$^0$ 3p$_{3/2}$ and Ru$^{<4+}$ 3p$_{3/2}$,[43,44] respectively. Notably, Ru 3p$_{3/2}$ spectra showed a 0.28 eV negative shift, corresponding to the accumulation of electrons at Ru centers. This bidirectional charge redistribution establishes a Mn → Ru electron transfer pathway.[32]

To further investigate the chemical state and coordination environment of the catalysts, X-ray absorption near-edge structure (XANES) analysis was performed. As shown in Figure 3b, the absorption edge on Ru/Mn$_{1.04}$-RuO$_2$ displayed a lower energy shift compared to Ru/RuO$_2$, indicating a lower valence state of Ru in the former.[43] Given that both samples incorporated identical Ru clusters, this suggested that the reduction in the oxidation state occurred for the Ru species within RuO$_2$. In conjunction with the XPS results, it was evident that the Mn atoms donated a portion of their electrons to the Ru atoms within RuO$_2$. For the XANES spectra at the Mn K-edge (Figure 3c), the pre-edge for Mn-RuO$_2$ was noticeably shifted toward lower binding energy compared to Ru/Mn$_{1.04}$-RuO$_2$, demonstrating that the average valence of Mn species in Ru/Mn$_{1.04}$-RuO$_2$ was higher.[32,41] According to the calculated valence states (Figure 3d), the average valence of the Mn species in Ru/Mn$_{1.04}$-RuO$_2$ was +2.74, whereas that in Mn-RuO$_2$ was +2.45.

To delve deeper into the coordination environment of the catalysts, an R-space EXAFS fitting analysis at the Ru and Mn K-edges was conducted. As shown in Figure 3e, a model-based EXAFS fit was performed on Ru/Mn$_{1.04}$-RuO$_2$, Mn-RuO$_2$, Mn foil, and Mn$_2$O$_3$. Ru/Mn$_{1.04}$-RuO$_2$ exhibited a peak at 1.40 Å, while Mn-RuO$_2$ showed a peak at 1.45 Å, both corresponding to Mn−O bonds.[32] This suggested that in Ru/Mn$_{1.04}$-RuO$_2$, single-atom Mn was exclusively doped into RuO$_2$ and coordinated with O atoms within RuO$_2$.[41,45] Compared to RuO$_2$, Ru/Mn$_{1.04}$-RuO$_2$ exhibited a decreased Ru−O bonding distance from 1.56 to 1.51 Å. Relative to Mn$_2$O$_3$, Ru/Mn$_{1.04}$-RuO$_2$ demonstrated a reduced Mn−O bonding distance from 1.44 to 1.40 Å (Figure 3e,f). These alterations were likely attributable to charge redistribution among Mn/Ru sites and O sites,[46,47] as further supported by the wavelet-transformed k2-weighted EXAFS spectra and Ru/Mn K-edge EXAFS oscillations for the involved catalysts (Figures S19−S22). Detailed fitting data are presented in Table S2.

A large specific surface area of catalysts facilitates reaction processes requiring rapid and efficient ion diffusion.[13] As shown in Figure S23, the Brunauer−Emmett−Teller (BET) surface area of Ru/Mn$_{1.04}$-RuO$_2$ was determined to be 117.22 m$^2$ g$^{-1}$, exceeding that of the other control samples. Temperature-programmed desorption of nitrogen on Mn-

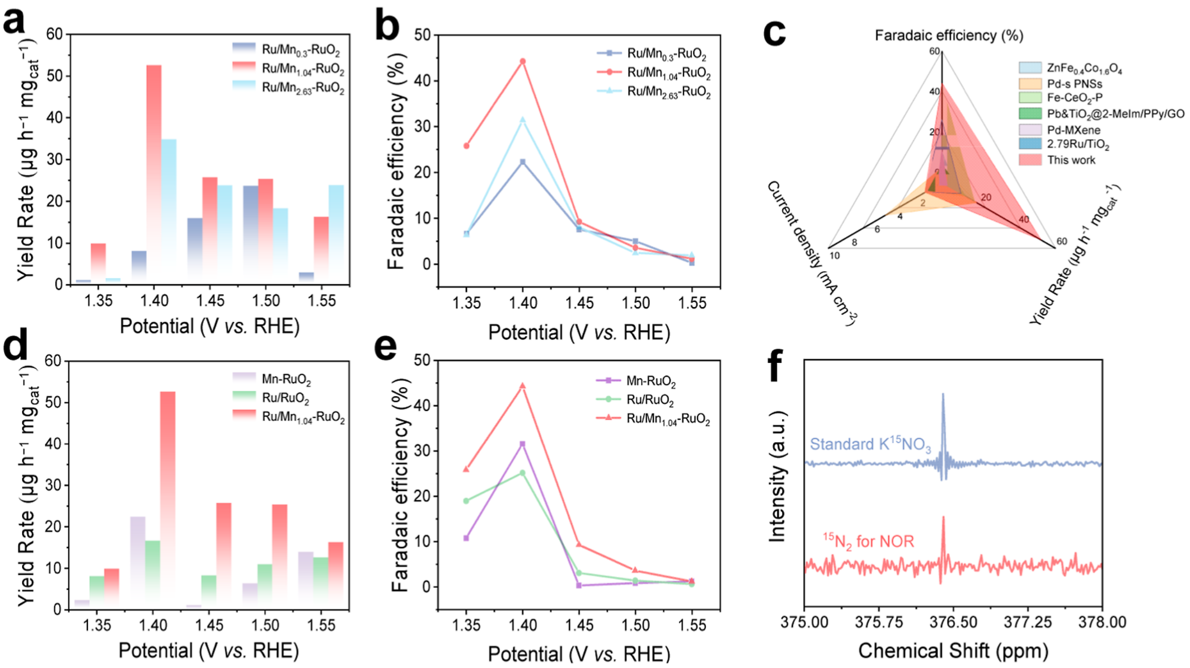

**Figure 4.** Electrocatalytic NOR performance of Ru/$Mn_x$-$RuO_2$. (a) Nitrate yields of Ru/$Mn_{1.04}$-$RuO_2$, Ru/$Mn_{0.3}$-$RuO_2$, and Ru/$Mn_{2.63}$-$RuO_2$. (b) Nitrate FE of Ru/$Mn_{1.04}$-$RuO_2$, Ru/$Mn_{0.3}$-$RuO_2$, and Ru/$Mn_{2.63}$-$RuO_2$. (c) Comparison of FE values, nitrate yields, and current density for Ru/$Mn_{1.04}$-$RuO_2$ with other reported NOR catalysts. (d) Nitrate yields of Ru/$Mn_{1.04}$-$RuO_2$, Ru/$RuO_2$, and Mn-$RuO_2$. (e) Nitrate FE of Ru/$Mn_{1.04}$-$RuO_2$, Ru/$RuO_2$, and Mn-$RuO_2$. (f) $^{15}N$ NMR spectra for standard samples of $^{15}NO_3^-$ and the test electrolyte produced from NOR using $^{15}N_2$ feeding gas.

$RuO_2$ and Ru/$Mn_x$-$RuO_2$ showed that the desorption peak for chemically adsorbed nitrogen (50−400 °C) shifted to lower temperatures as adsorption areas decreased, following the order Ru/$RuO_2$ > Ru/$Mn_{2.63}$-$RuO_2$ > Ru/$Mn_{1.04}$-$RuO_2$ > Mn-$RuO_2$ > Ru/$Mn_{0.3}$-$RuO_2$. This indicates the nitrogen binding strength order (Figure S24), with Ru/$Mn_{1.04}$-$RuO_2$ exhibiting moderate binding strength, suggesting balanced adsorption and desorption kinetics.[12,36]

**2.3. Electrochemical NOR Performance.** Controlled electrochemical experiments in H-type cells were systematically executed to assess the NOR performance of the Ru/$Mn_x$-$RuO_2$ catalysts (Figure S25). Linear sweep voltammetry (LSV) analyses revealed a marked improvement in current density for Ru/$Mn_{1.04}$-$RuO_2$ under $N_2$-saturated electrolyte conditions compared to Ar-saturated counterparts (Figure S26).[4,25] Quantitative ultraviolet−visible spectrophotometric analysis (Figure S27) confirmed nitrate as the primary oxidation product.[30,48] As demonstrated in Figure 4a,b, Ru/$Mn_{1.04}$-$RuO_2$ achieved peak performance at 1.40 V vs RHE, delivering a high FE of 44.29% and a nitrate production rate of 52.6 $\mu$g mg$^{-1}$ h$^{-1}$. These metrics substantially surpassed those of control catalysts (Ru/$Mn_{0.3}$-$RuO_2$ and Ru/$Mn_{2.63}$-$RuO_2$), positioning Ru/$Mn_{1.04}$-$RuO_2$ among state-of-the-art NOR electrocatalysts reported in contemporary literature (Figure 4c, Table S3).[18,21−24,30,48−50]

To identify active sites, comparative evaluations of the Mn-$RuO_2$ and Ru/$RuO_2$ controls were conducted (Figure 4d,e). While these materials exhibited measurable NOR activity (Figures S28 and S29), their inferior FE and yield metrics underscored the synergistic role of Ru clusters and Mn dopants in enhancing nitrate synthesis. Isotopic validation experiments employing $^{15}N_2$/$^{14}N_2$ feedstocks coupled with $^{15}N$ NMR spectroscopy (Figures 4f, S30, and S31) conclusively established molecular nitrogen as the nitrate precursor, evidenced by the characteristic $^{15}NO_3^-$ resonance at 376.4 ppm.[4,18,22] A comparison was made between the results obtained from ion chromatography (IC) and those from UV−vis detection (Figure S32). The findings revealed excellent agreement between the two methods with both yielding nearly identical nitrate production rates. This consistency highlighted the accuracy and reliability of the product quantification achieved in this work. These results confirmed that the nitrate produced was from the electrooxidation of nitrogen.

Catalytic durability assessments via chronoamperometry at 1.40 V demonstrated exceptional stability over five operational cycles, without obvious fluctuation in the FE or production rate (Figure S33). In addition, the structure and morphology of Ru/$Mn_{1.04}$-$RuO_2$ after the stability test were shown in Figures S34−S36. The SEM and TEM images obtained for the postcatalysis showed that there were virtually no changes in the morphology and structure of the material. Further, the results from HRTEM, XRD, and XPS analysis also showed no significant changes in the crystal structure of Ru/$Mn_{1.04}$-$RuO_2$ compared to those before the stability test, and metallic Ru was still present. The coupled plasma mass spectrometry analysis of the electrolyte after Ru/$Mn_{1.04}$-$RuO_2$ stability testing detected minimal metal leaching (30.482 ppb Ru, 0.256 ppb Mn; Table S4). These results all demonstrated that the material had outstanding stability during the NOR reaction process.

Electrochemical characterization revealed Ru/$Mn_{1.04}$-$RuO_2$'s superior double-layer capacitance (6.17 mF cm$^{-2}$, Figure S37), indicative of enhanced active site exposure. Kinetic advantages were further corroborated by its reduced Tafel slope (96.33 mV dec$^{-1}$ vs 104.66−113.12 mV dec$^{-1}$ for controls, Figure S38) and lower charge-transfer resistance (EIS, Figure S39), collectively affirming Mn doping's beneficial role in NOR kinetics. To provide a more accurate comparison of the intrinsic catalytic activities among the different catalysts

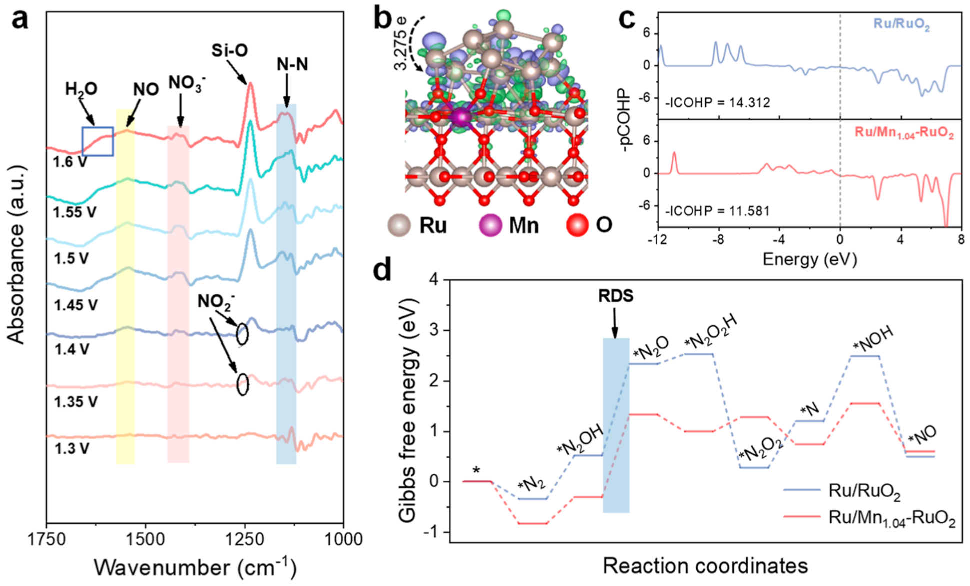

**Figure 5.** Mechanistic insights into NOR via in situ spectroscopy and DFT calculations. (a) In situ ATR-FTIR spectra of Ru/Mn$_{1.04}$-RuO$_2$ from 1.3 to 1.6 V in a N$_2$-saturated 0.1 M KOH electrolyte. (b) The charge density difference and Bader charge analysis of Ru/Mn$_{1.04}$-RuO$_2$. (c) The COHP for the N−N bond in *N$_2$ for both Ru/Mn$_{1.04}$-RuO$_2$ and Ru/RuO$_2$. (d) Calculated Gibbs free energy diagrams of NOR on Ru/Mn$_{1.04}$-RuO$_2$ and Ru/RuO$_2$.

evaluated, electrochemical active surface area (ECSA)-normalized yield data were calculated. The ECSA-normalized yields (Figure S40) demonstrated that Ru/Mn$_{1.04}$-RuO$_2$ exhibited robust nitrate production activity over a broad potential window, suggesting its intrinsically favorable catalytic properties.

### 2.4. Mechanistic Insights of NOR.

To interrogate the catalytic intermediates and substantiate the NOR mechanism, in situ attenuated total reflectance-Fourier transform infrared (ATR-FTIR) spectroscopy was implemented under dynamic reaction conditions to probe surface species on Ru/Mn$_{1.04}$-RuO$_2$. Spectral deconvolution (Figures 5a and S41) revealed distinct vibrational signatures at 1546 cm$^{-1}$ (N═O stretching), 1415 cm$^{-1}$ (*NO$_3^-$ symmetric vibration), and 1259 cm$^{-1}$ (asymmetric *NO$_2^-$ bending) upon polarization above 1.35 V vs RHE,[30,48,51,52] with an ancillary N−N stretching mode at 1130 cm$^{-1}$.[30,51] The concurrent detection of N═O and *NO$_2^-$ vibrational modes implicates *NO and *NO$_2^-$ as pivotal adsorbed intermediates on the Ru/Mn$_{1.04}$-RuO$_2$ governing the NOR pathway. Notably, the emergence of *NO$_3^-$-associated vibrations at 1.35 V, coupled with their potential-dependent intensification (1.35−1.50 V), signifies progressive *NO$_3^-$ accumulation via oxidative nitrogen conversion, outpacing its desorption-mediated nitrate release.[51] This potential-driven adsorbate enrichment was abruptly reversed at 1.55 V (Figure S42), concomitant with attenuated *NO$_3^-$ band intensity—a hallmark of competing OER dominance that disrupts *NO$_3^-$ stabilization at anodic extremes. These in situ spectroscopic insights collectively elucidate the potential-dependent adsorbate configurations and kinetic competition between NOR and OER on Ru/Mn$_{1.04}$-RuO$_2$, delineating a critical trade-off between intermediate stabilization and parasitic oxidation processes at elevated potentials.

To gain a deeper understanding of the influence of Mn doping on NOR, DFT calculations were conducted. Structural stability analysis based on postreaction characterization results confirmed that Ru clusters maintained their metallic state throughout NOR conditions, providing a critical foundation for model construction. Guided by these experimental observations, we established computationally tractable models of Ru/Mn$_{1.04}$-RuO$_2$ and Ru/RuO$_2$ (Figure S43). These models further revealed interfacial charge redistribution via differential charge density analysis (Figures 5b and S44). Charge depletion localized at Ru clusters contrasted with accumulation at RuO$_2$ interfaces, indicative of electron transfer from Ru to the oxide support, a phenomenon quantified by Bader charge analysis as 3.275 e for Mn-doped interfaces versus 3.189 e for undoped counterparts. In addition, the work functions (Φ) of the composite structure at interface regions were researched. As shown in Figure S45, the Φ of Mn-RuO$_2$ was 6.134 eV, which was significantly higher than that of the Ru clusters at 4.329 eV. This result further supported the direction of charge transfer at the interface, which was from the Ru clusters to the Mn-RuO$_2$ surface, well consistent with the findings of the charge density difference and Bader charge analysis.

To elucidate the impact of this charge transfer difference on the surface properties of Ru clusters, the surface electrostatic potentials for Ru/RuO$_2$ and Ru/Mn$_{1.04}$-RuO$_2$ were calculated (Figure S46). The results indicated that the electrostatic potential at the positive charge centers on the surface of Ru clusters in Ru/Mn$_{1.04}$-RuO$_2$ was higher than that in Ru/RuO$_2$, suggesting that Mn doping enhances the adsorption of reaction intermediates. Furthermore, crystal orbital Hamilton population (COHP) analysis of *N$_2$ adsorption (Figure 5c) demonstrated pronounced N−N bond weakening in Ru/Mn$_{1.04}$-RuO$_2$ (ICOHP = 11.581) relative to Ru/RuO$_2$ (14.312), confirming Mn doping's role in facilitating nitrogen activation.

To further unravel the reaction pathways on Ru clusters for NOR, the Gibbs free energy (Δ$G$) profiles for each intermediate were derived through thermodynamic calculations. The relative energy pathways for both Ru/Mn$_{1.04}$-RuO$_2$ and Ru/RuO$_2$ models are as determined by DFT (Figure 5d). The nitrogen molecule is adsorbed on the catalyst surface and oxidized by the first OH$^-$ ion to form *N$_2$OH. The second

$OH^-$ ion then abstracts a H atom, generating $H_2O$ and the $^*N_2O$ intermediate. Notably, the RDS for $Ru/RuO_2$ is the formation of $^*N_2O$, which involves a high reaction energy of 1.818 eV. In contrast, the RDS for $Ru/Mn_{1.04}$-$RuO_2$ exhibited a reduced reaction energy of 1.153 to 1.639 eV, indicating that the synergistic presence of Ru and Mn species more effectively enhances the activity of nitrate electrosynthesis. The observed discrepancy with an experiment potential of 1.40 V was not unexpected and did not invalidate the thermodynamic trends presented. The DFT results presented in this work were based on idealized surface models under implicit solvent and described the reaction thermodynamics at a microscopic scale on specific active sites. These computed reaction energies ($\Delta G$) did not account for complex experimental factors such as solvent reorganization, mass transport, possible dynamic restructuring of the catalyst surface, or large-scale catalysts. Nonetheless, DFT-based calculations were still valuable in offering mechanistic understanding and enabling meaningful comparisons of activity and selectivity across different catalytic systems or modifications. The final N−N bond cleavage occurs in the sixth step, where $^*N_2O_2$ decomposes into *N and releases $NO_2$. The resulting *N subsequently associates with $OH^-$ and evolves into *NO, which reacts with $O_2$ and $H_2O$ to form nitrate via a nonelectrochemical step in the NOR process (Figures S47 and S48). In addition, the reaction energies of both NOR and the OER were compared at the onset potential (1.153 V) for NOR on Ru/Mn-$RuO_2$. The results showed that at 1.153 V, all steps in the OER pathway were exothermic, suggesting that OER was thermodynamically more favorable at this onset potential. However, the reaction energy barriers for the RDS of both NOR and the OER revealed that the RDS for the OER has a significantly higher barrier compared to NOR (Figure S49). This result indicated that, while OER was thermodynamically favorable, the higher energy barrier of its RDS made the NOR pathway kinetically more favorable, resulting in higher selectivity for the NOR.

## 3. CONCLUSION

In summary, $Ru/Mn_{1.04}$-$RuO_2$ was meticulously designed and synthesized with the dual objectives of achieving high-efficiency nitrogen adsorption and activation while precisely modulating the OER. The $Ru/Mn_{1.04}$-$RuO_2$ catalyst demonstrated exceptional NOR activity, achieving a nitrate yield rate of 52.6 $\mu g\ mg^{-1}\ h^{-1}$ and a FE of 44.29%. Comprehensive systematic analyses revealed that Ru clusters serve as the primary active sites for activation of the N≡N triple bond during the NOR process. Both theoretical calculations and experimental results elucidated that Mn doping effectively suppresses the OER activity on $RuO_2$ while simultaneously enhancing nitrogen adsorption and activation on Ru clusters. This strategic modification was designed to improve the catalyst's selectivity toward NOR, thereby optimizing its efficiency for nitrogen oxidation. Collectively, this study presents a promising strategy for catalyst engineering and paves the way for innovative approaches to nitrogen fixation under ambient conditions of room temperature and atmospheric pressure.

## 4. METHODS

### 4.1. Synthesis of $Ru/Mn_x$-$RuO_2$.

$Ru/Mn_x$-$RuO_2$ was synthesized through a multistep process.[35] In a typical procedure, 0.086 g of $RuCl_3$ and 0.0339 g of $C_4H_6MnO_4\cdot 4H_2O$ were mixed in 75 mL of 1.0 M HCl and sonicated for 2 h. Carbon black (0.2 g) was then added and dispersed by stirring for 18 h under room temperature. Next, the mixture was dried by using a rotary evaporator, and the remaining powder was collected. The powder was annealed in a flowing $Ar/H_2$ (5% $H_2$) atmosphere at 900 °C for 2 h and then annealed in air at 450 °C for 3 h. After annealing, 50 mg of product was added to 20 mL of 1.0 M HCl and mixed at room temperature for 12 h to perform acid leaching and then centrifuged and washed with deionized water three times. Finally, the sample was dried at 80 °C in an oven for 12 h to obtain the catalyst. The resulting catalysts were denoted as $Ru/RuO_2$, $Ru/Mn_{0.3}$-$RuO_2$, $Ru/Mn_{1.04}$-$RuO_2$, and $Ru/Mn_{2.63}$-$RuO_2$ with Mn additions of 0, 0.017, 0.0339, and 0.0656 g, respectively.

### 4.2. Synthesis of Mn-$RuO_2$.

In a typical procedure, 0.086 g of $RuCl_3$ and 0.0339 g of $C_4H_6MnO_4\cdot 4H_2O$ were mixed in 75 mL of 1.0 M HCl and sonicated for 2 h. Carbon black (0.2 g) was then added and dispersed by stirring for 18 h under room temperature. Next, the mixture was dried by using a rotary evaporator, and the remaining powder was collected. The powder was annealed in air at 450 °C for 3 h. After annealing, 50 mg of product was added to 20 mL of 1.0 M HCl and mixed at room temperature for 12 h to perform acid leaching and then centrifuged and washed with deionized water three times. Finally, the sample was dried at 80 °C in an oven for 12 h to obtain the catalyst.

### 4.3. Characterizations.

The morphologies and compositions of samples were observed with a field-emission scanning electron microscope (SU-8010), transmission electron microscopy (TEM, HT7700) images, high-resolution TEM (HRTEM, Tecnai G2 F20 S-TWIN) images, and selected-area electron diffraction (SAED) patterns obtained on a JEM-2100 electron microscope (JEM-2100, 200 kV) equipped with an energy-dispersive X-ray spectrometer, operating at 120 kV. High-angle annular dark-field scanning TEM (HAADF-STEM) imaging of samples was performed on a Carl Zeiss Libra 120 with double spherical aberration correctors. Surface area and porosity analyzer (Quantachrome, Autosorb-iQ-MP) of samples were measured by Brunauer−Emmett−Teller (BET, Micromeritics ASAP 2020) measurements with $N_2$ desorption/adsorption isotherms. The crystal structures of the samples were characterized by X-ray powder diffraction (XRD, SHIMADZU XRD-6000) and Raman spectra (Raman, LabRAM HR Evolution). The chemical environments of samples were measured with X-ray photoelectron spectroscopy (XPS, Escalab 250Xi). The BL12B2 station in Japan and the BL20U station in the Shanghai Synchrotron Radiation Facility (SSRF) were employed for collecting X-ray absorption fine structure (XAFS) data of Ru and Mn elements. The purity of $N_2$ was verified by mass spectrometry (GCMS-QP2020 NX).

### 4.4. Electrochemical Measurements.

All electrochemical measurements were performed on a CHI 760E electrochemical workstation (Shanghai Chenhua Instrument Co., China) using a three-electrode with the graphite rod and Hg/HgO electrode as counter and reference electrodes. The working electrode was prepared before the electrochemical test. 5 mg of catalyst was dispersed into 1000 $\mu$L of solution consisting of 950 $\mu$L of ethanol and 50 $\mu$L of 5 wt % Nafion solution to achieve a homogeneous ink by ultrasonication for at least 30 min. Next, 50 $\mu$L of catalyst ink was pipetted onto carbon paper ($1 \times 1$ $cm^2$) with a loading amount of 0.25 mg $cm^{-2}$. The potentials reported in this work were converted to the RHE scale via calibration with the following equation: E (vs RHE) = $E$ (vs Hg/HgO) + 0.098 + 0.059 × pH. All experiments were carried out at room temperature (25 °C). For NOR, the electrolyte was purged with $N_2$ gas for 30 min before the measurements. The potentiostatic test was conducted in a $N_2$-saturated 0.1 M KOH solution in a H cell, which was separated by a Nafion membrane. Pure $N_2$ gas was continuously fed into the anodic compartment during the experiments. All CV or LSV curves were recorded without $iR$ compensation. The ECSA was determined by ECSA = $C_{dl}/C_s$, where $C_{dl}$ is the electrical double-layer capacitor, which was measured from double-layer charging curves using cyclic voltammograms in a non-Faradaic region, and $C_s$ is the specific capacitance of the sample. In this study, a general specific capacitance of $C_s$ = 0.06 mF $cm^{-2}$ was used based on typical reported values.[43,45]

**4.5. Nitrate Determination.** The produced nitrate in the electrolyte was measured using an ultraviolet spectrophotometer method.[22] First, 4 mL of electrolyte was taken out from the electrolytic cell. Then, 0.08 mL of 1.0 M HCl and 0.008 mL of 0.8 wt % sulfamic acid solution were added into the solution. The absorption spectrum was tested using an ultraviolet−visible spectrophotometer, and the absorption intensities at wavelengths of 220 and 275 nm were recorded. The final absorbance value was calculated by the equation $A = A_{220\ nm} - 2A_{275\ nm}$. The concentration absorbance curve was calculated using a series of standard potassium nitrate solutions. After 2 h of reaction, the absorption spectra of the resulting solution were acquired with an ultraviolet−visible spectrophotometer (SHIMADZU, Japan). The rate of $NO_3^-$ formation was calculated using the following equation:[53]

$$\text{yield rate} = (62c_{NO_3^-} \times V)/(t \times m_{cat})$$

The Faradaic efficiency was calculated as follows:

$$\text{Faradaic efficiency} = (5F \times c_{NO_3^-} \times V)/Q$$

where $c_{NO_3^-}$ is the measured $NO_3^-$ concentration, $V$ is the volume of electrolyte, and $t$ is the electrolysis time (2 h). $F$ is the Faraday constant (96,485 C $mol^{-1}$), $Q$ is the total charge passed through the electrode, and $t$ is the electrolysis time.

**4.6. $^{15}N$ Isotopic Labeling Experiment.** For $^{15}N_2$ isotope (Wuhan Newradar Special Gas Co., Ltd., 99 atom % $^{15}N$) labeling experiment, after 50 h of NOR with $^{15}N_2$ feeding gas, the obtained $^{15}NO_3^-$-containing electrolyte was analyzed by $^{15}N_2$ nuclear magnetic resonance (NMR, JEOL ECA400). $D_2O$ was applied as the solvent, and the reaction time of each NMR test was 11 h with 11,000 scans. Note that the test electrolytes were subjected to the concentration treatment up to 0.5 mL before NMR analysis.

**4.7. In Situ ATR-FTIR Tests.** The in situ ATR-FTIR study was carried out on an Invenio-R spectrometer equipped with a mercury cadmium telluride (MCT) detector cooled with liquid nitrogen. The Au-coated Si hemispherical prism (20 mm in diameter, MTI Corporation) was used as the conductive substrate for catalysts and the IR reflection element. The catalysts were dispersed into the mixture solution consisting of ethyl alcohol and 0.5 wt % Nafion solution and stirred overnight, and the loading amount of the as-prepared catalyst on the prism was 0.1 mg $cm^{-2}$. In all tests, the Pt electrode and Ag/AgCl electrode were used as counter and reference electrodes, respectively. A 0.1 M KOH solution saturated with $N_2$ was used as the electrolyte. The spectrum was given in absorbance units defined as Abs = $-\lg(R/R_0)$, where $R$ and $R_0$ represent reflected in situ ATR-FTIR intensities corresponding to the single-beam spectra of the sample and reference, respectively. In this experiment, a chronopotentiometry test was used at different potentials without in situ ATR-FTIR correction. The potential was set from 1.3 to 1.6 V, which was collected during the test.

**4.8. DFT Calculations.** All calculations of structure relaxation and electronic properties were performed by the Vienna ab initio simulation package with projector-augmented wave pseudopotential (PAW).[54,55] Spin-polarized calculations were employed in this work to determine the electronic spin property of materials, and to explore its magnetic configuration, we performed energy comparisons for different magnetic configurations (Table S5). The nonmagnetic configuration was adopted in following research. The Perdew−Burke−Ernzerhof (PBE) functional at the generalized gradient approximation (GGA) level was used to treat the exchange−correlation.[56,57] To compare the effects of different van der Waals (vdW) corrections on $N_2$ adsorption, we performed calculations using the zero-damping DFT-D3 method, the DFT-D3 method with Becke−Johnson damping, the DFT-D2 method of Grimme, and a method without vdW corrections for $N_2$ adsorption on different metals (Figure S50). The three vdW correction methods yielded similar ranges of adsorption energy corrections for $N_2$ adsorption on different metals. In this work, the zero-damping DFT-D3 method of Grimme was employed for van der Waals (vdW) interactions.[58,59] A cutoff energy was set to 450 eV, and $k$-points were sampled using the gamma-centered mesh with a reciprocal space resolution of $2\pi \times 0.05$ Å$^{-1}$ for structural optimization calculations, respectively,[60−62] which ensured that the energy convergence criteria were fulfilled (Figures S51 and S52). For the calculation of the DOS, a higher $k$-point grid density of $2\pi \times 0.04$ Å$^{-1}$ was adopted, which already met the energy convergence accuracy requirements. The convergence threshold was set to be $1 \times 10^{-5}$ eV/atom in energy and 0.02 eV/Å in force. The $RuO_2(110)$ slab was constructed from tetragonal phase $RuO_2$ (ID: MP-825 at materialsproject.org). And in the structural optimization calculations, the two layers of atoms at the bottom were fixed (lattice parameters in Table S6). Guided by experimental observations, we established computationally tractable models of Ru/$Mn_{1.04}$-$RuO_2$ and Ru/$RuO_2$; namely, the configuration of the Ru cluster supported on the $RuO_2$ surface was constructed by a simplified pyramid-like cluster containing 11 Ru atoms on the $RuO_2(110)$ surface. To avoid any interactions due to the use of periodic boundary conditions, a vacuum separation between two neighboring slabs was set as 15 Å. The dipole correction was employed for all of the surface configurations. The solvent effect was described by VASPsol code with the dielectric constant of 80.[63] For the localized d-electrons in Ru and Mn, we employed the DFT + $U$ method, which corrected the self-interaction error and provided a more accurate description of the electronic and magnetic properties of these elements. Specifically, we applied the on-site interaction parameter $U_{eff}$ of 4.88 eV for Ru[64] and 3.06 eV for Mn.[65] To describe the electrochemical synthesis of nitrate, the computational hydrogen electrode (CHE) model was used to establish a free energy profile, as proposed by Nørskov and co-workers.[66] The charge density difference was based on the formula $\Delta\rho = \rho_{RuO_2+Ru\ cluster} - \rho_{RuO_2} - \rho_{Ru\ cluster}$. The climbing image nudged elastic band

(CLNEB) method was used to calculate the RDS energy barrier with a total of 5 images.[67,68]

## ■ ASSOCIATED CONTENT

### Supporting Information

The Supporting Information is available free of charge at https://pubs.acs.org/doi/10.1021/acscatal.5c01568.

> Adsorption free energy, ICOHP analysis, comparison of vdW methods of $*N_2$, OER mechanism and thermodynamics, convenience of computational parameters (including cutoff energy and *k*-points), electronic properties of materials, materials synthesis and characterization (including XRD, SEM, TEM, EDX, XPS, XAS spectra, BET, $N_2$-TPD, in situ ATR-FTIR spectra, etc.), electrocatalytic H-cell device and performance (LSV, UV−vis, CV, $^{15}N$ isotopic labeling experiment, MS and IC, Tafel slope, EIS, and ECSA), stability tests (recycling tests, XRD, SEM, TEM, EDX XPS, etc.), models and DFT calculation results (composition structures, interface charge density, NOR mechanism, and reaction kinetics), and other additional supplementary electrochemical data (PDF)

## ■ AUTHOR INFORMATION

### Corresponding Authors

**Dashuai Wang** − *Key Laboratory of Biomass Chemical Engineering of Ministry of Education, College of Chemical and Biological Engineering, Zhejiang University, Hangzhou 310027, China; Institute of Zhejiang University—Quzhou, Quzhou 324000, China*; Email: dswang@zju.edu.cn

**Yang Hou** − *Key Laboratory of Biomass Chemical Engineering of Ministry of Education, College of Chemical and Biological Engineering, Zhejiang University, Hangzhou 310027, China; Zhejiang University Hydrogen Energy Institute, Hangzhou 310027, China; School of Biological and Chemical Engineering, NingboTech University, Ningbo 315100, China*; orcid.org/0000-0001-9795-8503; Email: yhou@zju.edu.cn

### Authors

**Haixia Zeng** − *Key Laboratory of Biomass Chemical Engineering of Ministry of Education, College of Chemical and Biological Engineering, Zhejiang University, Hangzhou 310027, China*

**Cheng-Jie Yang** − *Department of Physics, Tamkang University, New Taipei City 25137, Taiwan*

**Chung-Li Dong** − *Department of Physics, Tamkang University, New Taipei City 25137, Taiwan*; orcid.org/0000-0002-4289-4677

**Weixiao Lin** − *Research and Testing Centre of Material School of Materials Science and Engineering, Wuhan University of Technology, Wuhan 430070, China*

**Xiahan Sang** − *Research and Testing Centre of Material School of Materials Science and Engineering, Wuhan University of Technology, Wuhan 430070, China*; orcid.org/0000-0002-2861-6814

**Bin Yang** − *Key Laboratory of Biomass Chemical Engineering of Ministry of Education, College of Chemical and Biological Engineering, Zhejiang University, Hangzhou 310027, China*; orcid.org/0000-0002-5136-9743

**Zhongjian Li** − *Key Laboratory of Biomass Chemical Engineering of Ministry of Education, College of Chemical and Biological Engineering, Zhejiang University, Hangzhou 310027, China*; orcid.org/0000-0002-3685-381X

**Siyu Yao** − *Key Laboratory of Biomass Chemical Engineering of Ministry of Education, College of Chemical and Biological Engineering, Zhejiang University, Hangzhou 310027, China*; orcid.org/0000-0001-5660-5269

**Qinghua Zhang** − *Key Laboratory of Biomass Chemical Engineering of Ministry of Education, College of Chemical and Biological Engineering, Zhejiang University, Hangzhou 310027, China*; orcid.org/0000-0003-1350-6388

**Jianguo Lu** − *State Key Laboratory of Silicon Materials, Key Laboratory for Biomedical Engineering of Ministry of Education, School of Materials Science and Engineering, Zhejiang University, Hangzhou 310027, China*; orcid.org/0000-0001-6183-6336

**Lecheng Lei** − *Key Laboratory of Biomass Chemical Engineering of Ministry of Education, College of Chemical and Biological Engineering, Zhejiang University, Hangzhou 310027, China*

**Yuanyuan Li** − *Wallenberg Wood Science Center, Department of Fiber and Polymer Technology, KTH Royal Institute of Technology, Stockholm 10044, Sweden*; orcid.org/0000-0002-1591-5815

**Raul D. Rodriguez** − *Tomsk Polytechnic University, Tomsk 634050, Russia*; orcid.org/0000-0003-4016-1469

Complete contact information is available at: https://pubs.acs.org/10.1021/acscatal.5c01568

### Author Contributions

All authors have given approval to the final version of the manuscript.

### Notes

The authors declare no competing financial interest.

## ■ ACKNOWLEDGMENTS

The authors thank the financial support from the National Natural Science Foundation of China (22211530045, 22425805, U22A20432, 22278364, 22178308, 22238008), the National Key Research and Development Program of China (2022YFB4002100), the development project of Zhejiang Province's "Jianbing" and "Lingyan" (2023C01226, 2024C01056), the Fundamental Research Funds for the Central Universities (226-2024-00060), the Key Technology Breakthrough Program of Ningbo "Science and Innovation Yongjiang 2035" (2024H024), and the Research Funds of Institute of Zhejiang University-Quzhou (IZQ2021RCZX040, 1ZQ2023KJ1002).

## ■ REFERENCES

(1) Liu, Y.; Cheng, M.; He, Z.; Gu, B.; Xiao, C.; Zhou, T.; Guo, Z.; Liu, J.; He, H.; Ye, B.; Pan, B.; Xie, Y. Pothole-rich Ultrathin $WO_3$ Nanosheets that Trigger N≡N Bond Activation of Nitrogen for Direct Nitrate Photosynthesis. *Angew. Chem., Int. Ed.* **2019**, *58*, 731−735.

(2) Honkala, K.; Hellman, A.; Remediakis, I. N.; Logadottir, A.; Carlsson, A.; Dahl, S.; Christensen, C. H.; Nørskov, J. K. Ammonia Synthesis from First-Principles Calculations. *Science* **2005**, *307*, 555−558.

(3) Medford, A. J.; Hatzell, M. C. Photon-Driven Nitrogen Fixation: Current Progress, Thermodynamic Considerations, and Future Outlook. *ACS Catal.* **2017**, *7*, 2624−2643.

(4) Wang, Y.; Yu, Y.; Jia, R.; Zhang, C.; Zhang, B. Electrochemical synthesis of nitric acid from air and ammonia through waste utilization. *Natl. Sci. Rev.* **2019**, *6*, 730−738.

(5) Tang, C.; Qiao, S.-Z. How to explore ambient electrocatalytic nitrogen reduction reliably and insightfully. *Chem. Soc. Rev.* **2019**, *48*, 3166−3180.

(6) Zheng, W.; Yang, X.; Li, Z.; Yang, B.; Zhang, Q.; Lei, L.; Hou, Y. Designs of Tandem Catalysts and Cascade Catalytic Systems for $CO_2$ Upgrading. *Angew. Chem., Int. Ed.* **2023**, *62*, No. e202307283.

(7) Kou, Z.; Liu, Y.; Cui, W.; Yang, B.; Li, Z.; Rodriguez, R. D.; Zhang, Q.; Dong, C.-L.; Sang, X.; Lei, L.; Zhang, T.; Hou, Y. Electronic structure optimization of metal−phthalocyanine via confining atomic Ru for all-pH hydrogen evolution. *Energy Environ. Sci.* **2024**, *17*, 1540−1548.

(8) Tang, C.; Zheng, Y.; Jaroniec, M.; Qiao, S. Z. Electrocatalytic Refinery for Sustainable Production of Fuels and Chemicals. *Angew. Chem., Int. Ed.* **2021**, *60*, 19572−19590.

(9) Peng, X.; Zeng, L.; Wang, D.; Liu, Z.; Li, Y.; Li, Z.; Yang, B.; Lei, L.; Dai, L.; Hou, Y. Electrochemical C-N coupling of $CO_2$ and nitrogenous small molecules for the electrosynthesis of organonitrogen compounds. *Chem. Soc. Rev.* **2023**, *52*, 2193−2237.

(10) Lin, H.; Wei, J.; Guo, Y.; Li, Y.; Lu, X.; Zhou, C.; Liu, S.; Li, Y.-y. $Bi_1$-$CuCo_2O_4$ Hollow Carbon Nanofibers Boosts $NH_3$ Production from Electrocatalytic Nitrate Reduction. *Adv. Funct. Mater.* **2024**, *34*, 2409696.

(11) Li, Y.; Wei, J.; Lin, H.; Guo, Y.; Lu, X.; Liu, S.; Liu, H.; Tang, M.; Zhou, J.; Li, Y.-y. Hollow Square Ni-Doped Copper Oxide Catalyst Boosting Electrocatalytic Nitrate Reduction. *ACS Catal.* **2025**, *15*, 1672−1683.

(12) Li, Y.; Ji, Y.; Zhao, Y.; Chen, J.; Zheng, S.; Sang, X.; Yang, B.; Li, Z.; Lei, L.; Wen, Z.; Feng, X.; Hou, Y. Local Spin-State Tuning of Iron Single-Atom Electrocatalyst by S-Coordinated Doping for Kinetics-Boosted Ammonia Synthesis. *Adv. Mater.* **2022**, *34*, No. e2202240.

(13) Li, Y.; Li, J.; Huang, J.; Chen, J.; Kong, Y.; Yang, B.; Li, Z.; Lei, L.; Chai, G.; Wen, Z.; Dai, L.; Hou, Y. Boosting Electroreduction Kinetics of Nitrogen to Ammonia via Tuning Electron Distribution of Single-Atomic Iron Sites. *Angew. Chem., Int. Ed.* **2021**, *60*, 9078−9085.

(14) Wang, Z.; Zhang, Q.; Wang, H.; Sun, C.; Li, X.; He, H.; Wang, J.; Zhao, Y.; Zhang, X. Efficient Nitrate Generation through Electrochemical $N_2$ Oxidation with Nickel Oxyhydroxide Decorated Copper Hydroxide Driven by Solar Cells. *Small* **2023**, *19*, 2301438.

(15) Xie, M.; Tang, S.; Li, Z.; Wang, M.; Jin, Z.; Li, P.; Zhan, X.; Zhou, H.; Yu, G. Intermetallic Single-Atom Alloy In-Pd Bimetallene for Neutral Electrosynthesis of Ammonia from Nitrate. *J. Am. Chem. Soc.* **2023**, *145*, 13957−13967.

(16) Chen, J. G.; Crooks, R. M.; Seefeldt, L. C.; Bren, K. L.; Bullock, R. M.; Darensbourg, M. Y.; Holland, P. L.; Hoffman, B.; Janik, M. J.; Jones, A. K.; Kanatzidis, M. G.; King, P.; Lancaster, K. M.; Lymar, S. V.; Pfromm, P.; Schneider, W. F.; Schrock, R. R. Beyond fossil fuel-driven nitrogen transformations. *Science* **2018**, *360*, No. eaar6611.

(17) Wang, Y.; Li, T.; Yu, Y.; Zhang, B. Electrochemical Synthesis of Nitric Acid from Nitrogen Oxidation. *Angew. Chem., Int. Ed.* **2022**, *61*, No. e202115409.

(18) Kuang, M.; Wang, Y.; Fang, W.; Tan, H.; Chen, M.; Yao, J.; Liu, C.; Xu, J.; Zhou, K.; Yan, Q. Efficient Nitrate Synthesis via Ambient Nitrogen Oxidation with Ru-Doped $TiO_2/RuO_2$ Electrocatalysts. *Adv. Mater.* **2020**, *32*, 2002189.

(19) Kong, Y.; Li, Y.; Sang, X.; Yang, B.; Li, Z.; Zheng, S.; Zhang, Q.; Yao, S.; Yang, X.; Lei, L.; Zhou, S.; Wu, G.; Hou, Y. Atomically Dispersed Zinc(I) Active Sites to Accelerate Nitrogen Reduction Kinetics for Ammonia Electrosynthesis. *Adv. Mater.* **2022**, *34*, 2103548.

(20) Zhang, Y.; Du, F.; Wang, R.; Ling, X.; Wang, X.; Shen, Q.; Xiong, Y.; Li, T.; Zhou, Y.; Zou, Z. Electrocatalytic fixation of $N_2$ into $NO_3^-$: electron transfer between oxygen vacancies and loaded Au in $Nb_2O_{5-x}$ nanobelts to promote ambient nitrogen oxidation. *J. Mater. Chem. A* **2021**, *9*, 17442−17450.

(21) Fang, W.; Du, C.; Kuang, M.; Chen, M.; Huang, W.; Ren, H.; Xu, J.; Feldhoff, A.; Yan, Q. Boosting efficient ambient nitrogen oxidation by a well-dispersed Pd on MXene electrocatalyst. *Chem. Commun.* **2020**, *56*, 5779−5782.

(22) Han, S.; Wang, C.; Wang, Y.; Yu, Y.; Zhang, B. Electrosynthesis of Nitrate via the Oxidation of Nitrogen on Tensile-Strained Palladium Porous Nanosheets. *Angew. Chem., Int. Ed.* **2021**, *60*, 4474−4478.

(23) Li, T.; Han, S.; Wang, C.; Huang, Y.; Wang, Y.; Yu, Y.; Zhang, B. Ru-Doped Pd Nanoparticles for Nitrogen Electrooxidation to Nitrate. *ACS Catal.* **2021**, *11*, 14032−14037.

(24) Dai, C.; Sun, Y.; Chen, G.; Fisher, A. C.; Xu, Z. J. Electrochemical Oxidation of Nitrogen towards Direct Nitrate Production on Spinel Oxides. *Angew. Chem., Int. Ed.* **2020**, *59*, 9418−9422.

(25) Zhang, L.; Cong, M.; Ding, X.; Jin, Y.; Xu, F.; Wang, Y.; Chen, L.; Zhang, L. A Janus Fe-$SnO_2$ Catalyst that Enables Bifunctional Electrochemical Nitrogen Fixation. *Angew. Chem., Int. Ed.* **2020**, *59*, 10888−10893.

(26) Zhang, S.; Shi, T.; Li, K.; Sun, Q.; Lin, Y.; Zheng, L. R.; Wang, G.; Zhang, Y.; Yin, H.; Zhang, H. Ambient Electrochemical Nitrogen Fixation over a Bifunctional Mo−(O−$C_2$)$_4$ Site Catalyst. *J. Phys. Chem. C* **2022**, *126*, 965−973.

(27) Guo, Y.; Zhang, S.; Zhang, R.; Wang, D.; Zhu, D.; Wang, X.; Xiao, D.; Li, N.; Zhao, Y.; Huang, Z.; Xu, W.; Chen, S.; Song, L.; Fan, J.; Chen, Q.; Zhi, C. Electrochemical Nitrate Production via Nitrogen Oxidation with Atomically Dispersed Fe on N-Doped Carbon Nanosheets. *ACS Nano* **2022**, *16*, 655−663.

(28) Xu, F.; Liu, X.; Zhang, L.; Guo, M.; Li, M.; Ding, X.; Zhang, L. Revealing and Optimizing the Dialectical Relationship Between NOR and OER: Cation Vacancy Engineering Enables $RuO_2$ With Unanticipated High Electrochemical Nitrogen Oxidation Performance. *Adv. Energy Mater.* **2023**, *13*, 2300615.

(29) Nie, Z.; Zhang, L.; Ding, X.; Cong, M.; Xu, F.; Ma, L.; Guo, M.; Li, M.; Zhang, L. Catalytic Kinetics Regulation for Enhanced Electrochemical Nitrogen Oxidation by Ru-Nanoclusters-Coupled $Mn_3O_4$ Catalysts Decorated with Atomically Dispersed Ru Atoms. *Adv. Mater.* **2022**, *34*, No. e2108180.

(30) Li, T.; Han, S.; Cheng, C.; Wang, Y.; Du, X.; Yu, Y.; Zhang, B. Sulfate-Enabled Nitrate Synthesis from Nitrogen Electrooxidation on a Rhodium Electrocatalyst. *Angew. Chem., Int. Ed.* **2022**, *61*, No. e202204541.

(31) Wan, H.; Bagger, A.; Rossmeisl, J. Limitations of Electrochemical Nitrogen Oxidation toward Nitrate. *Phys. Chem. Lett.* **2022**, *13*, 8928−8934.

(32) Wang, K.; Wang, Y.; Yang, B.; Li, Z.; Qin, X.; Zhang, Q.; Lei, L.; Qiu, M.; Wu, G.; Hou, Y. Highly active ruthenium sites stabilized by modulating electron-feeding for sustainable acidic oxygen-evolution electrocatalysis. *Energy Environ. Sci.* **2022**, *15*, 2356−2365.

(33) Yu, J.; He, Q.; Yang, G.; Zhou, W.; Shao, Z.; Ni, M. Recent Advances and Prospective in Ruthenium-Based Materials for Electrochemical Water Splitting. *ACS Catal.* **2019**, *9*, 9973−10011.

(34) Chang, S. H.; Danilovic, N.; Chang, K.-C.; Subbaraman, R.; Paulikas, A. P.; Fong, D. D.; Highland, M. J.; Baldo, P. M.; Stamenkovic, V. R.; Freeland, J. W.; Eastman, J. A.; Markovic, N. M. Functional links between stability and reactivity of strontium ruthenate single crystals during oxygen evolution. *Nat. Commun.* **2014**, *5*, 4191.

(35) Wu, Z. Y.; Chen, F. Y.; Li, B.; Yu, S. W.; Finfrock, Y. Z.; Meira, D. M.; Yan, Q. Q.; Zhu, P.; Chen, M. X.; Song, T. W.; Yin, Z.; Liang, H. W.; Zhang, S.; Wang, G.; Wang, H. Non-iridium-based electrocatalyst for durable acidic oxygen evolution reaction in proton exchange membrane water electrolysis. *Nat. Mater.* **2023**, *22*, 100−108.

(36) Yu, M.; Fan, G.; Liu, J.; Xu, W.; Li, J.; Cheng, F. Self-supported Mo-doped $TiO_2$ electrode for ambient electrocatalytic nitrogen oxidation. *Electrochim. Acta* **2022**, *435*, 141333.

(37) Boakye, F. O.; Harrath, K.; Zhang, D.; You, Y.; Zhang, W.; Wang, Z.; Zhang, H.; Zhu, J.; Long, J.; Zhu, J.; Yasin, G.; Owusu, K. A.; Tabish, M.; Zhang, L.; Wang, D.; Shi, X.; Jiang, Z.; Wu, B.; Mai, L.; Zhao, W. Synergistic Engineering of Dopant and Support of Ru

Oxide Catalyst Enables Ultrahigh Performance for Acidic Oxygen Evolution. *Adv. Funct. Mater.* **2024**, *34*, 2408714.

(38) Yan, S.; Liao, W.; Zhong, M.; Li, W.; Wang, C.; Pinna, N.; Chen, W.; Lu, X. Partially oxidized ruthenium aerogel as highly active bifunctional electrocatalyst for overall water splitting in both alkaline and acidic media. *Appl. Catal., B* **2022**, *307*, 121199.

(39) Xu, Q.; Zhang, J.; Zhang, H.; Zhang, L.; Chen, L.; Hu, Y.; Jiang, H.; Li, C. Atomic heterointerface engineering overcomes the activity limitation of electrocatalysts and promises highly-efficient alkaline water splitting. *Energy Environ. Sci.* **2021**, *14*, 5228−5259.

(40) Wang, Z.; Xiao, B.; Lin, Z.; Xu, Y.; Lin, Y.; Meng, F.; Zhang, Q.; Gu, L.; Fang, B.; Guo, S.; Zhong, W. $PtSe_2$/Pt Heterointerface with Reduced Coordination for Boosted Hydrogen Evolution Reaction. *Angew. Chem., Int. Ed.* **2021**, *60*, 23388−23393.

(41) Li, Y.; Li, Z.; Shi, K.; Luo, L.; Jiang, H.; He, Y.; Zhao, Y.; He, J.; Lin, L.; Sun, Z.; Sun, G. Single-Atom Mn Catalysts via Integration with Mn Sub Nano-Clusters Synergistically Enhance Oxygen Reduction Reaction. *Small* **2023**, *20*, 2309727.

(42) Li, Q.; Zhao, L.; Zhu, Z.; Xiong, P.; Zuo, J.; Chen, J. S.; Li, R.; Wu, R. Engineering atomically dispersed Mn and Fe sites on hollow nitrogen-doped carbon for high-performance Zn-air batteries. *J. Colloid Interface Sci.* **2025**, *682*, 460−466.

(43) Zhu, Y.; Klingenhof, M.; Gao, C.; Koketsu, T.; Weiser, G.; Pi, Y.; Liu, S.; Sui, L.; Hou, J.; Li, J.; Jiang, H.; Xu, L.; Huang, W. H.; Pao, C. W.; Yang, M.; Hu, Z.; Strasser, P.; Ma, J. Facilitating alkaline hydrogen evolution reaction on the hetero-interfaced Ru/$RuO_2$ through Pt single atoms doping. *Nat. Commun.* **2024**, *15*, 1447.

(44) Huang, K.; Lin, C.; Yu, G.; Du, P.; Xie, X.; He, X.; Zheng, Z.; Sun, N.; Tang, H.; Li, X.; Lei, M.; Wu, H. Ru/Se-$RuO_2$ Composites via Controlled Selenization Strategy for Enhanced Acidic Oxygen Evolution. *Adv. Funct. Mater.* **2022**, *33*, 2211102.

(45) Kim, K.; Kim, G.; Jeong, T.; Lee, W.; Yang, Y.; Kim, B.-H.; Kim, B.; Lee, B.; Kang, J.; Kim, M. Activating the Mn Single Atomic Center for an Efficient Actual Active Site of the Oxygen Reduction Reaction by Spin-State Regulation. *J. Am. Chem. Soc.* **2024**, *146*, 34033−34042.

(46) Coropceanu, V.; Chen, X.-K.; Wang, T.; Zheng, Z.; Brédas, J.-L. Charge-transfer electronic states in organic solar cells. *Nat. Rev. Mater.* **2019**, *4*, 689−707.

(47) Nguyen, T. X.; Liao, Y.-C.; Lin, C.-C.; Su, Y.-H.; Ting, J.-M. Advanced High Entropy Perovskite Oxide Electrocatalyst for Oxygen Evolution Reaction. *Adv. Funct. Mater.* **2021**, *31*, 2101632.

(48) Wang, S.; Liu, S.; Cheng, Q.; Wang, M.; Liu, H.; Zhang, L.; Qian, T.; Yan, C. "Hole" traps promoting direct nitrate synthesis within flux controlled $N_2$-rich circumstance. *Chem. Eng. J.* **2023**, *455*, 140669.

(49) Mao, H.; Sun, Y.; Li, H.; Wu, S.; Liu, D.; Li, H.; Li, S.; Ma, T. Synergy of $Pd_2^+/S_2^-$-Doped $TiO_2$ Supported on 2-Methylimidazolium-Functionalized Polypyrrole/Graphene Oxide for Enhanced Nitrogen Electrooxidation. *Adv. Mater.* **2024**, *36*, 2313155.

(50) Mao, H.; Sun, Y.; Li, H.; Li, S.; Liu, D.; Sun, Y.; Wu, S.; Li, H.; Ma, T.; Zhang, R. Electrosynthesis of nitrate by Pd and $TiO_2$ nanoparticles anchored on 2-methylimidazolium functionalized polypyrrole/graphene oxide. *Electrochim. Acta* **2024**, *482*, 143978.

(51) Li, T.; Han, S.; Wang, Y.; Zhou, J.; Zhang, B.; Yu, Y. A Spectroscopic Study on Nitrogen Electrooxidation to Nitrate. *Angew. Chem., Int. Ed.* **2023**, *62*, No. e202217411.

(52) Guo, H.; Guo, Z.; Chu, K.; Zong, W.; Zhu, H.; Zhang, L.; Liu, C.; Liu, T.; Hofkens, J.; Lai, F. Polymer-Confined Pyrolysis Promotes the Formation of Ultrafine Single-Phase High-Entropy Alloys: A Promising Electrocatalyst for Oxidation of Nitrogen. *Adv. Funct. Mater.* **2023**, *33*, 2308229.

(53) Guo, M.; Fang, L.; Zhang, L.; Li, M.; Cong, M.; Guan, X.; Shi, C.; Gu, C.; Liu, X.; Wang, Y.; Ding, X. Pulsed Electrocatalysis Enabling High Overall Nitrogen Fixation Performance for Atomically Dispersed Fe on $TiO_2$. *Angew. Chem., Int. Ed.* **2023**, *62*, No. e202217635.

(54) Kresse, G.; Furthmüller, J. Efficient iterative schemes for ab initio total-energy calculations using a plane-wave basis set. *Phys. Rev. B: Condens. Matter Mater. Phys.* **1996**, *54*, 11169−11186.

(55) Kresse, G.; Furthmüller, J. Efficiency of ab-initio total energy calculations for metals and semiconductors using a plane-wave basis set. *Comput. Mater.* **1996**, *6*, 15−50.

(56) Perdew, J. P.; Burke, K.; Ernzerhof, M. Generalized Gradient Approximation Made Simple. *Phys. Rev. Lett.* **1996**, *77*, 3865−3868.

(57) Hammer, B.; Hansen, L. B.; Nørskov, J. K. Improved adsorption energetics within density-functional theory using revised Perdew-Burke-Ernzerhof functionals. *Phys. Rev. B: Condens. Matter Mater. Phys.* **1999**, *59*, 7413−7421.

(58) Grimme, S.; Antony, J.; Ehrlich, S.; Krieg, H. A consistent and accurate ab initio parametrization of density functional dispersion correction (DFT-D) for the 94 elements H-Pu. *J. Chem. Phys.* **2010**, *132*, 154104.

(59) Qin, Y.; Yu, T.; Deng, S.; Zhou, X.-Y.; Lin, D.; Zhang, Q.; Jin, Z.; Zhang, D.; He, Y.-B.; Qiu, H.-J.; He, L.; Kang, F.; Li, K.; Zhang, T.-Y. $RuO_2$ electronic structure and lattice strain dual engineering for enhanced acidic oxygen evolution reaction performance. *Nat. Commun.* **2022**, *13*, 3784.

(60) Wang, Y.; Lei, X.; Zhang, B.; Bai, B.; Das, P.; Azam, T.; Xiao, J.; Wu, Z.-S. Breaking the Ru-O-Ru Symmetry of a $RuO_2$ Catalyst for Sustainable Acidic Water Oxidation. *Angew. Chem., Int. Ed.* **2024**, *63*, No. e202316903.

(61) Wang, Y.; Yang, R.; Ding, Y.; Zhang, B.; Li, H.; Bai, B.; Li, M.; Cui, Y.; Xiao, J.; Wu, Z.-S. Unraveling oxygen vacancy site mechanism of Rh-doped $RuO_2$ catalyst for long-lasting acidic water oxidation. *Nat. Commun.* **2023**, *14*, 1412.

(62) Yu, J.; Zeng, Y.; Jin, Q.; Lin, W.; Lu, X. Hydrogenation of $CO_2$ to Methane over a Ru/$RuTiO_2$ Surface: A DFT Investigation into the Significant Role of the $RuO_2$ Overlayer. *ACS Catal.* **2022**, *12*, 14654−14666.

(63) Gauthier, J. A.; Dickens, C. F.; Chen, L. D.; Doyle, A. D.; Nørskov, J. K. Solvation Effects for Oxygen Evolution Reaction Catalysis on $IrO_2$(110). *J. Phys. Chem. C* **2017**, *121*, 11455−11463.

(64) Latimer, A. A.; Abild-Pedersen, F.; Nørskov, J. K. A Theoretical Study of Methanol Oxidation on $RuO_2$(110): Bridging the Pressure Gap. *ACS Catal.* **2017**, *7*, 4527−4534.

(65) Gong, L.; Zhang, D.; Lin, C.-Y.; Zhu, Y.; Shen, Y.; Zhang, J.; Han, X.; Zhang, L.; Xia, Z. Catalytic Mechanisms and Design Principles for Single-Atom Catalysts in Highly Efficient $CO_2$ Conversion. *Adv. Energy Mater.* **2019**, *9*, 1902625.

(66) Nørskov, J. K.; Rossmeisl, J.; Logadottir, A.; Lindqvist, L.; Kitchin, J. R.; Bligaard, T.; Jónsson, H. Origin of the Overpotential for Oxygen Reduction at a Fuel-Cell Cathode. *J. Phys. Chem. B* **2004**, *108*, 17886−17892.

(67) Henkelman, G.; Uberuaga, B. P.; Jónsson, H. A climbing image nudged elastic band method for finding saddle points and minimum energy paths. *J. Chem. Phys.* **2000**, *113*, 9901−9904.

(68) Henkelman, G.; Jónsson, H. Improved tangent estimate in the nudged elastic band method for finding minimum energy paths and saddle points. *J. Chem. Phys.* **2000**, *113*, 9978−9985.